JOURNAL OF GEOPHYSICAL RESEARCH: SPACE PHYSICS, VOL. 118, 3377–3393, doi:10.1002/jgra.50204, 2013

Oxygen-hydrogen differentiated observations from TWINS: The 22 July 2009 storm

P. W. Valek,[1,2] J. Goldstein,[1,2] D. J. McComas,[1,2] R. IIie,[3] N. Buzulukova,[4,5] M.-C. Fok,[6] and J. D. Perez[7]

Received 2 November 2012; revised 21 February 2013; accepted 23 February 2013; published 25 June 2013.

[1] The 22 July 2009 magnetic storm is the first significant storm during the emergence of the recent prolonged solar cycle minimum. This moderate storm (minimum Dst approximately ≤ -78 nT) has received a good deal of attention in the community. We present here global observations of the H and O populations in the inner magnetosphere using Energetic Neutral Atom (ENA) observations from the TWINS mission. We develop and provide the methodology for separating H and O ENAs, based on mass dependent differences in the pulse height distributions of the microchannel plate (MCP) based detectors. We present the first composition separated H and O ENA images at central energies of 16 and 32 keV. We also show that TWINS has sufficient angular resolution to separate the High Altitude Emissions (HAEs) from the Low Altitude Emissions (LAEs). We observe that all ENA emissions in this energy range quickly rise, but the O ENAs have a larger relative increase, and stay at elevated levels much longer, well into the recovery phase.

Citation: Valek, P. W., J. Goldstein, D. J. McComas, R. IIie, N. Buzulukova, M.-C. Fok, and J. D. Perez (2013), Oxygen-hydrogen differentiated observations from TWINS: The 22 July 2009 storm, *J. Geophys. Res. Space Physics*, *118*, 3377–3393, doi:10.1002/jgra.50204.

1. Introduction

[2] The 22 July 2009 magnetic storm is the first moderate storm during the emergence from the prolonged minimum of solar cycle at the beginning of solar cycle 24. It is also the largest storm since December of 2006. This moderate storm (minimum Dst approximately ≤ -78 nT) has received a good deal of attention in the community [*Valek et al*., 2010; *Fok et al*., 2010; *Glocer et al*., 2011; *Keesee et al*., 2012; *Perez et al*., 2012]

[3] *Valek et al*. [2010] presented the first Energetic Neutral Atom (ENA) images of this storm from the Two Wide-angle Imaging Neutral-atom Spectrometers (TWINS) [*McComas et al*., 2009]. Flown aboard two spacecraft in Molniya orbits, TWINS allows for continuous observations of the inner magnetosphere with at least one ENA imager and stereo observations multiple times a day. *Valek et al*. [2010] showed that emissions from high altitudes (due to charge exchange of ring current ions with neutral hydrogen in the exosphere at high altitudes) were markedly different from those from lower altitudes where the ENAs are generated at <500 km (due to charge exchange of ions from the loss cone with neutral oxygen in the upper atmosphere) [*Roelof*, 1997; *Bazell et al*., 2010]. Low altitude ENAs emit from a narrow range of pitch angles compared to the broader range emitted by the high altitude ENAs (see *Goldstein et al*. [2012a, 2012b] for TWINS measurements of global high altitude ENA pitch angle anisotropy)

[4] Previous studies have referred to the low altitude emissions as LAEs, and the emissions for high altitudes as Ring Current Emissions, or RCEs authors [*Buzulukova et al*., 2010; *Fok et al*., 2010; *Valek et al*., 2010]. Since the ring current is a major source of these high altitude ENA emissions, this nomenclature is reasonable, but other regions of the magnetosphere (e.g., plasmasheet) also contribute to these high altitude emissions. We have chosen to use the naming convention of *McComas et al*. [2012] and refer to the high altitude emissions as HAEs.

[5] During the 22 July storm, the LAEs were seen to peak about an hour earlier than the HAEs. Using the thick target and large target approximation from *Bazell et al*. [2010], the observed ENA energy spectra of the LAEs and HAEs, respectively, were transformed to show the energy spectra of the parent ion populations[*Valek et al*., 2010]. Due the lack of composition measurements, *Valek et al*. [2010] had to assume that the ENAs observed were all from H. The spectral shape of the LAE and HAE ion populations were quite different, with the LAEs showing an energy dispersion not seen in the HAEs. High-energy LAEs were seen first; the lower-energy LAEs were seen to fill in over tens of minutes. Interestingly, a similar time history was observed in the LAEs by *McComas et al*. [2012] for the 5 April 2010 substorm.

[1]Southwest Research Institute, San Antonio, Texas, USA.
[2]University of Texas, San Antonio, Texas, USA.
[3]Los Alamos Laboratory, Los Alamos, New Mexico, USA.
[4]CRESST and Geospace Physics Laboratory, NASA Goddard Space Flight Center, Greenbelt, Maryland, USA.
[5]Department of Astronomy, University of Maryland, College Park, Maryland, USA.
[6]Geospace Physics Laboratory, NASA Goddard Space Flight Center, Greenbelt, Maryland, USA.
[7]Auburn University, Auburn, Alabama, USA.

Corresponding author: P. W. Valek, Southwest Research Institute, San Antonio, TX 78228, USA. (PValek@swri.edu)

2169-9380/13/10.1002/jgra.50204

This article was corrected on 1 JUL 2015. See the end of the full text for details.

[6] *Fok et al*. [2010] modeled the 22 July 2009 storm and compared those results with the ENA emissions seen by the TWINS and in situ ion measurements made by THEMIS [*Angelopoulos*, 2008]. Simulation runs were performed with both static and time-varying magnetic fields. They concluded that while a time-varying B is important, "global convection" dominates if Dst is less than approximately −50 nT

[7] *Glocer et al*. [2011] studied the rapid rebuilding of the outer radiation belts during this storm. The refilling of the outer belt typically takes days, but in this event, the refilling occurred within only a few hours. These authors used a combination of observations from the Akebono satellite, NOAA POES and GOES 11 satellites, and the in situ monitors aboard the TWINS 1 spacecraft along with modeling results using the coupled Radiation Belt Environment (RBE) model and Block-Adaptive-Tree Solar wind Roe-type Upwind Scheme (BATS-R-US) code. *Glocer et al*. [2011] showed results indicating that the rapid enhancement of MeV electrons is due to a dipolarization of the magnetic field which transports the electrons earthward and energizes them through conservation of the first and second adiabatic invariants.

[8] *Perez et al*. [2012] showed the evolution of the energy spectrum of the ring current for the 22 July storm. They performed inversions of the TWINS ENA images of this storm to determine the global ion energy spectrum. The energy spectra obtained during the time period when the LAEs were dominant showed a peak energy that evolved from approximately 20 keV at 0344 UT to between 10 and 15 keV at 0544 UT consistent with what was inferred in *Valek et al*. [2010]. The energy spectrum from the deconvolved ENA images later in the early recovery phase of the storm showed reasonable agreement when compared to in situ measurements from THEMIS.

[9] Missing from our current understanding of this storm (and the magnetosphere at this time), especially in the global context, is the contribution and distribution of oxygen to storm dynamics. O^+ can be a significant component during storm times. *Daglis et al*. [1993] and *Daglis* [1997] showed that during large storms, the energy density of the ring current can be dominated by O^+, and even for moderate storms, the O^+ energy density can increase significantly. *Mitchell et al*. [2003] showed that the O ENA content, measured at >50–100 keV by IMAGE/HENA, increases in bursts during substorm onset during storms. *Fok et al*. [2006] used coupled kinetic-MHD code for modeling of O HAEs during magnetospheric substorm. It was shown that bursts of oxygen ENA observed by *Mitchell et al*. [2003] come from nonadiabatic heating of O^+ stored in the magnetotail before substorm onset. Recent modeling work has further shown the importance of the inclusion of O^+ in the dynamics of storms [*Glocer et al*., 2009a, 2009b; *Welling et al*., 2011].

[10] In this study, we present here the first Oxygen ENA images measured by TWINS. The TWINS energy range extends far below that of HENA and allows us to image and understand the physics of this critical ion component separately for the bulk H over the plasma and low-energy ranges of energetic particles for the first time. Brief descriptions of the TWINS ENA images and the method used to determine H and O ENA content from this data set are given in sections 2.1 and 2.2. A more complete discussion of the composition determination of the TWINS data set is presented in section A. Observations of the measured ENA composition of the 22 July 2009 moderate storm are presented in section 3. We observe that the ENA emissions in this energy range quickly rise, but the O ENAs have a larger relative increase, and stay at elevated levels much longer, well into the recovery phase. Discussion and conclusions are given in section 4.

2. Methodology

2.1. TWINS Overview

[11] The TWINS mission [*McComas et al*., 2009] includes two identical Energetic Neutral Atom (ENA) imagers flown aboard two separate spacecraft in Molniya orbits (inclination of 63°, orbital period of 12 h, and apogee ~7.2 R_E) to image the inner magnetosphere. The phasing of the orbits is such that the TWINS sensors provide essentially continuous ENA observations from at least one of the TWINS spacecraft and stereoscopic imaging for approximately 2 h twice each day.

[12] The TWINS ENA imagers are based upon the slit camera concept [*McComas et al*., 1998] originally flown as the MENA instrument [*Pollock et al*., 2000] on the IMAGE mission [*Burch*, 2000]. Two sensor heads are used to acquire an instantaneous 1-D spatial image across the full energy spectrum of the ENAs. The imager is rotated back and forth in a windshield wiper motion to fill the full field of view (FOV). The TWINS FOV is an approximately nadir pointing cone with a half width of 60°. Neutral atoms are detected and recorded at very high angular resolution (~1°) with $\Delta E/E \leq 1.0$ for H atoms. Full images are taken in 60 s typically every 72 s over an energy range from <1 keV/amu up to ~100 keV/amu. See section A of *McComas et al*. [2012] for a full description of how the ENAs are processed to generate images.

[13] The TWINS instrument uses ultrathin carbon foils of a nominal 0.5 μg cm^{-2} mounted at the aperture to make a coincidence time of flight (TOF) measurement. Ultrathin carbon foils (typically 0.5 to 3.5 μg cm^{-2}), mounted on highly transmissive grids, have been used successfully in a wide variety of space missions [*McComas et al*., 2004]. As the primary ENA passes through the foil, emitted secondary electrons are accelerated to a microchannel plate (MCP) detector where they provide a timing start pulse. The primary ENA is then measured in a different region of the same MCP, producing the timing stop pulse. The ENA trajectory measurements are obtained using the detected positions of an ENA and its associated secondary electrons. Complete details about how the TWINS instruments work are provided in the TWINS mission paper [*McComas et al*., 2009].

2.2. Composition Determination

[14] Both H^+ and O^+ in the magnetosphere charge exchange efficiently with the exosphere and upper atmospheric neutrals producing H and O ENAs. ENA composition identification is determined by analyzing the mass dependent differences in the pulse height distributions of the MCP based detectors. This technique has been used successfully on the HENA [*Mitchell et al*., 2003] and magnetosphere imaging instrument (MIMI) [*Mitchell et al*., 2004] ENA imagers to look at higher energy (> 50–100 keV) O ENAs. The stop pulse in the TWINS velocity measurement is from the impact of the primary ENA. The pulse height varies as a function of mass, and this variation is what the HENA and MIMI instruments

use to determine ENA composition. For TWINS, however, the variation of the pulse height between the H and O stop pulses for the lower energies measured is fairly small. Therefore, instead, we use the pulse height distribution generated by the secondary electrons emitted from the carbon foils to determine the composition of the ENA signal. A brief overview of the technique used for composition separation is given here, with a more complete description provided in section A.

[15] As the primary ENA passes through the carbon foil, secondary electrons are liberated and accelerated toward the MCP detector. The mean number of electrons emitted from the foil exit surface (n) increases with increased ENA mass and velocity [*Gruntman et al*., 1990; *Ritzau and Baragiola*, 1998]. The (mostly secondary) electrons leave the carbon surface with an energy small (approximately few eV) compared to the energy imparted by the accelerating potential (~1.1 keV) inside the detector section. The n electrons liberated from the carbon foil impact the MCP with nearly the same energy. Due to spreading from the initial exit directions from the foil and space charge effects, the n electrons strike the MCPs with a spacing generally larger than the pore-to-pore distances of tens of microns. Therefore, each of these n electrons can start cascades in independent groups of pores in the MCPs. Because the MCP pores are essentially separate electron multipliers, the pulse height from n electrons will be, to zeroth order, n times that of a single electron.

[16] An incident beam, even of a pure mono-energetic, single species ENAs produces a broad distribution of pulse heights owing to the statistical nature of the MCP multiplication process. Additionally, while the average pulse height for H and O are separated in TWINS, the distributions also have significant overlap, so it is not possible to distinguish the species of the incident ENA on an event by event basis. Rather, for a given velocity range, the measured pulse height distribution is fit to a linear combination of characteristic pulse height distributions of the H and O ENAs, determined during the instrument flight calibration [*McComas et al*., 2009]. Once the numbers of H and O events are determined, species specific geometric factors are applied to determine the flux of H and O to produce composition separated ENA images.

[17] An aspect of the TWINS images, which results from using start foils for timing, is that the incident particles undergo energy straggling and angle scattering as they pass though the foils (see *Valek et al*. [2010] for how these effect the imaging). The magnitudes of these effects are functions of (1) the foil properties, (2) the foil thickness, and (3) the incident energy and species of the particle passing though the foil [*Funsten et al*., 1993; *Allegrini et al*., 2006]. For particles arriving at the carbon foils with the same incident angle and energy, more massive particles experience larger energy loss and angular scattering. Because of this, the TWINS instrument will make higher resolution measurements of the H ENAs than of the O ENAs. The magnitude of the energy straggling and angular scattering is reduced for all species as the foil thickness is reduced. To minimize the energy straggling and angular scattering, carbon foils as thin as those reliably flown to date are used in TWINS (nominal thickness ~0.5 mg/cm^2) [*McComas et al*., 2004].

[18] Since TWINS viewing is collimated in one spatial dimension and actively imaged in the other dimension (radial in TWINS images—perpendicular to the collimated direction), angular scattering effects are limited to the imaging dimension. Intense ENA emissions can scatter and create artifacts that appear as extended emissions in the imaging direction. Lower-energy and more massive ENAs will produce the largest scattering artifacts. Low-energy oxygen ENAs will scatter across a wide angular range even if they are coming from a localized region in space. For this initial paper on O ENAs, we only present ENA images where the O is at sufficiently high energy (16 and 32 keV) so that the scattering is small enough to still allow high resolution images (~ 4°).

3. Observations

[19] On 22 July, the IMF turned strongly southward, and the proton density increased to a peak value of ~50 cm^{-3}. Starting around 0430 UT, the IMF transitioned to a strong negative By at 0600 and then again to negative Bz at 0800 UT. The proton speed (not shown) increased steadily from ~300 km/s before 22 July to speeds of ~500 km/s on 23 July. The solar wind dynamic pressure increased to a peak value of ~ 12 nPa around 0500 UT. See Figure 1 for a summary of the environmental conditions during this storm.

[20] The duration and strength of the IMF Bz has been shown to be the main driver of magnetic storms [*Gonzales et al*., 1994; *Zhang et al*., 2004; *Zhang et al*., 2006]. The IMF must be < -5 nT for at least 2 h for a moderate storm (-30 nT $>$ Dst > -100 nT) at the 80% occurrence level. The solar wind conditions meet this criterion for this storm (Figure 1).

[21] As in *Perez et al*. [2012], we classify the 22 July 2009 storm as a Co-rotating Interaction Region (CIR) driven storm primarily due to the nonsteady north/south component of the interplanetary magnetic field (Figure 1, red trace in top panel). CIRs are large-scale structures in the heliosphere that generally produce weak storms defined as those with minimum SYM/H > -100 nT. CIR storms also tend to lack a sudden storm commencement (SSC) and have long recovery phases ($>$ 24 h). The 22 July 2009 storm meets all of these criteria. A review of CIR storms is given in *Tsurutani et al*. [2006].

[22] The main phase of the magnetic storm was seen to begin at around 0200 UT and reached a minimum of -95 nT in Sym-H. This double dip storm had its first minimum at 0600 UT. The IMF Bz turned northward at ~ 0600 UT for about 1 h and then southward again, resulting in a second minimum of nearly the same magnitude as the first at 0900 UT. There is an initial recovery phase with a rapid increase of Sym-H from 0900–1100 UT where the long duration decay commences.

[23] Figure 2 shows a sequence of O and H ENA images taken just prior to the storms main phase, at peak of the storm, during the middle of the storm, and during the slow recovery. Each image includes data integrated over 30 min with the start of the time indicated by the label; the energy bands have a width of 100%. Figure 2a shows Sym-H with the time of the images indicated with vertical bars. The 16 keV images are shown in Figure 2b, and 32 keV images are shown in Figure 2c.

[24] Figure 2 gives an overview of the dynamics of the H and O ENAs through this storm. Just prior to the storm onset (0058 UT), the brightest ENA emissions observed are H LAEs near dusk (i.e., bright emissions at the limb near the purple field lines). The brightest ENA emissions are seen at the peak of the storm (0530 UT).The brightest feature in

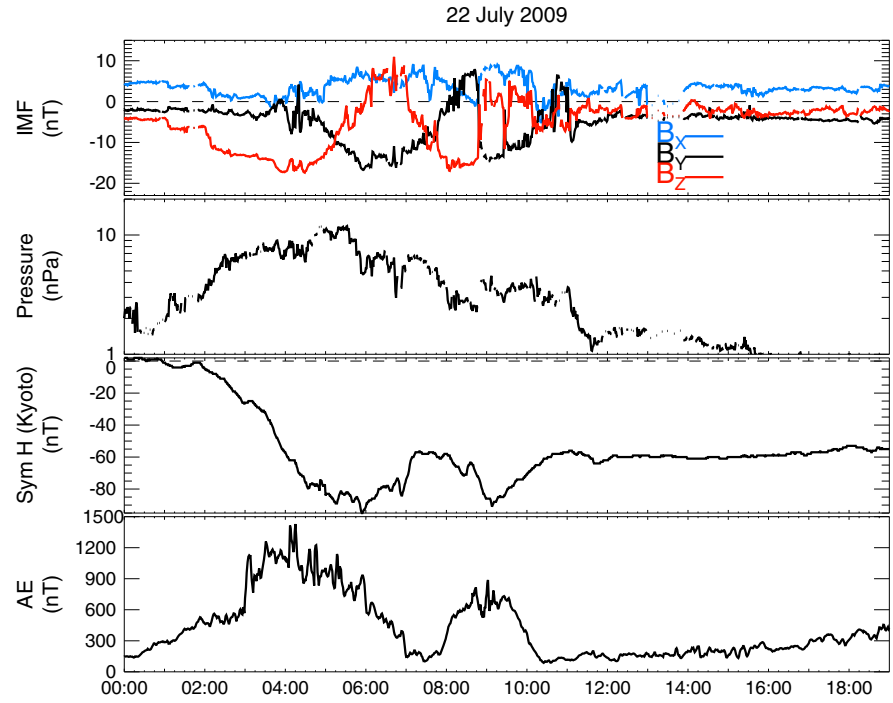

Figure 1. Environmental conditions during the 22 July storm. Panels are (from top) IMF, solar wind pressure, Sym-H, and AE. All times are in UT.

the H ENA images at 0530 UT is the LAEs, seen at dusk (foot print of purple field line). For the O ENA image, the HAE emissions are approximately as bright as the LAEs. Later (0829 UT), we see increased emissions in both H and O ENAs. The ring current (HAEs) fills in with a more extended local time coverage for O than for H ENAs.

[25] In the final set of images during the recovery (1258 UT), the HAEs are seen to be on the dusk side, with larger relative O to H emissions than the pre-storm (0058 UT) levels. The average ENA flux across the full TWINS H 16 keV image increases from 1.1×10^{-2} to 2.9×10^{-2} $(\mathrm{eV\,cm^2\,sr\ s})^{-1}$ (a factor of 2.6) between the 0058 and 1258 images. The average ENA flux across the full O 16 keV image increases from 1.9×10^{-5} to 2.3×10^{-3} $(\mathrm{eV\,cm^2\,sr\,s})^{-1}$ (a factor of 121) between the 0058 and 1258 images. For the 32 keV images, the average H ENA flux increases from 3.2×10^{-3} to 1.1×10^{-2} $(\mathrm{eV\,cm^2\,sr\,s})^{-1}$ (a factor of 3.4), and the average O ENA flux increases from 1.2×10^{-5} to 1.3×10^{-3} (a factor of 92).

[26] The measured counts are distributed between H and O counts based on the fitting parameter A in equation A2. The number of fitted counts is not required to an integer value. Maps of the counting uncertainties can then be produced using $\sigma = \sqrt{n}$. Figure 3 is a map of the scaled counting error for the ENA images shown in Figure 2.

[27] The energy dependence of the charge exchange cross sections is important when comparing the H and O ENA emissions. The charge exchange cross sections for H^+ on H changes significantly between the 16 and 32 keV energy bands used in this paper, while the O^+ on H charge exchange cross section is has less variation. Figure 4 shows the charge exchange cross sections as a function of energy from *Lindsay and Stebbings* [2005]. The energy bands used in the ENA images in this paper are shown in blue (16 keV) and yellow (32 keV), with the overlap in green. It is worth noting that for the 16 keV energy band, the average cross sections for H and O are nearly equal, but for the 32 keV band, the O cross section is significantly larger that the H cross section. Because of the energy dependence of the charge exchange cross section, the fraction of O/H ENA emissions will generally be larger with increased energy than the parent ion populations.

[28] As discussed above, the ENA emissions observed by TWINS can be separated into HAEs (greater than approximately 500 km) where the probability of multiple collisions is very low (called "optically thin") and LAEs, where ions precipitate into the upper atmosphere ($<$ 500 km) and undergo multiple charge exchanges (called optically thick). At low altitudes, the LAEs are generated by mirroring ions and come from a narrow range of pitch angles [*Roelof*, 1997; *Pollock et al.*, 2009; *Bazell et al.*, 2010]. Because of this, observations of the LAEs have a strong dependence on the location of the TWINS spacecraft. An optically thick approximation is required to account for multiple collisions producing LAEs [*Bazell et al.*, 2010]. The neutral density in the upper atmosphere is much larger than further out in the exosphere, and therefore, the LAEs appear brighter in the TWINS ENA images than the ring current for similar flux of ions.

[29] For both HAEs and LAEs, the ENA flux is dominated by H. Just prior to the onset of the storm (0058 UT in Figure 2), TWINS observed the brightest ENA emissions coming from the H LAE. The O emissions at this time are fairly dim, localized to the post midnight sector and from relatively near the earth ($L \sim < 4$) (Figure 2). At ~0200 UT, the storm begins, and the flux of both LAE and HAE ENAs increases rapidly.

[30] Figure 5 shows a sequence of images from 0230 to 0400 UT, which coincides with the main phase of the storm. The error maps for this time are shown in Figure 6. At 0230

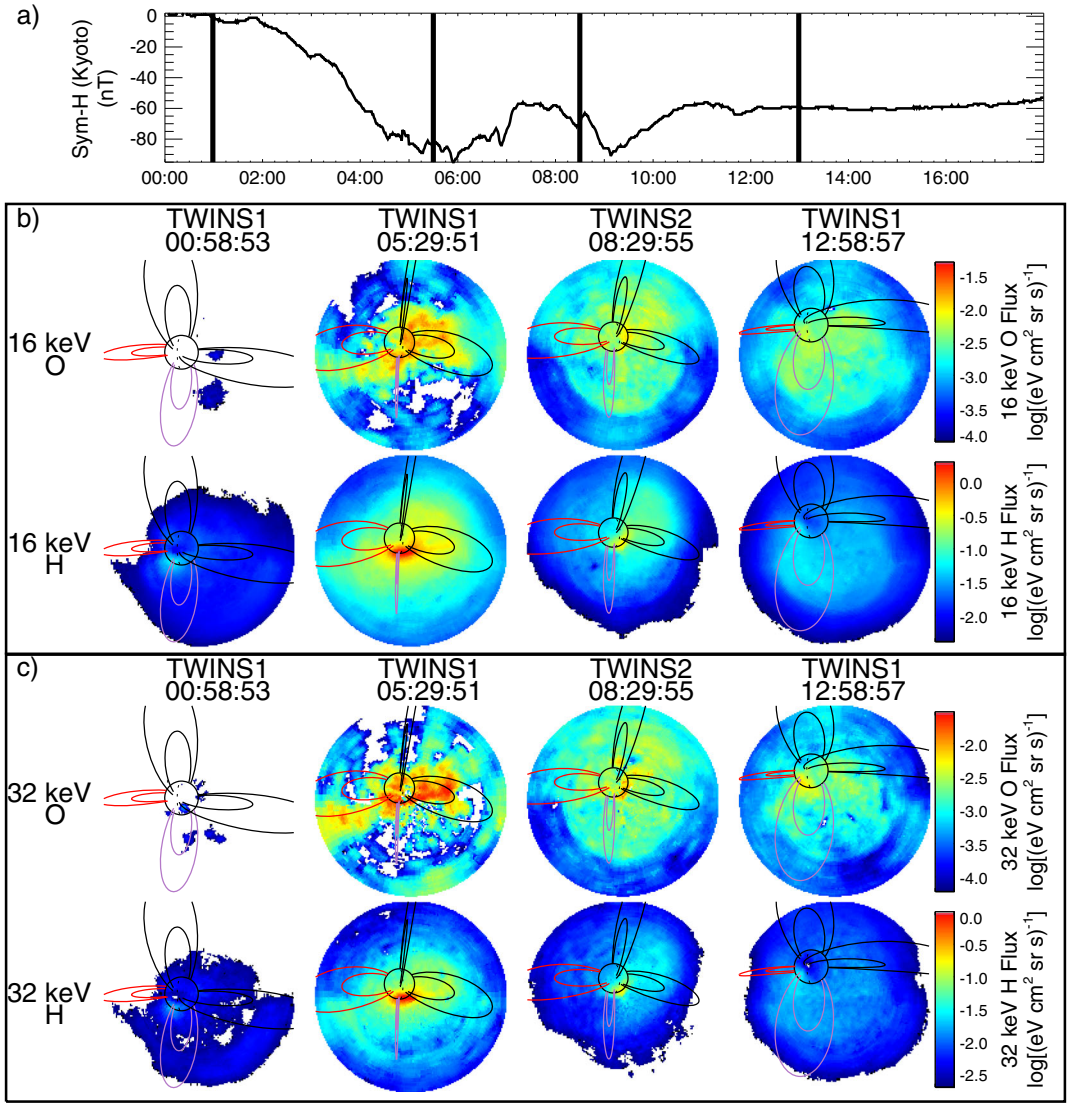

Figure 2. TWINS observations of H and O ENAs through the storm. For context, the figure shows the (a) Sym-H plot, with the times of the (b and c) images indicated with vertical lines. Each of the ENA images shown consist of data integrated over a 30 min time period, with the start time indicated. The H and O logarithmic color bars cover a different range, but all images of the same species and energy use the same color bar. The Earth's limb and dipole field lines at $L = 4$ and 8 are drawn in to aid viewing. The sunward lines are in red, and duskward lines are in purple.

UT, the H LAEs were seen in the afternoon / dusk sector, where the O LAE emission was still dim, with a peak near midnight. Over the hour and a half shown in Figure 5, the LAE emissions for both species are seen to rapidly increase. The O LAE initially is observed on the night side but transitions to the dusk side with the H LAEs. At 0400 UT, the peak of the O and H LAEs are both seen at dusk. The O LAEs extend for nearly 12 h of local time as opposed to the H LAEs that are more peaked near dusk.

[31] Care must be taken when interpreting the LAE observations due to strong viewing geometry effects. Due to their narrow range of pitch angles [*Roelof*, 1997; *Pollock et al*., 2009; *Bazell et al*., 2010], LAEs from a limited range of local times will be observable from a given location in space. The spatial probability of viewing LAEs is given the "emissivity function" and is described by *Bazell et al*. [2010]. The emissivity function has a crescent shape, generally centered 12 h of local time from the location of the TWINS spacecraft. See *Bazell et al*. [2010, Figures 8–10] for examples of emissivity functions for TWINS. For the images in Figure 5, the emissivity function is peaked near dusk.

[32] Later in the storm at 0830 UT (Figure 2), both strong HAE and LAE emissions are observed, and a well-formed ring current is seen in both the H and O emissions. The TWINS 2 spacecraft is in a prime location at this time to see LAEs in the pre-midnight sector. The H ENAs observed by TWINS 2 show both bright LAEs and HAEs. The H LAEs are brighter than the H HAEs at this time. However, the HAE and LAE emissions are of approximately equal brightness in the O ENA image. Since the LAE production process occurs where the neutral density is greater, this indicates that the line-of-sight integrated O^+ ion populations responsible for the HAE is greater in the ring current than for the narrow region where O^+ ions are mirroring in the upper atmosphere.

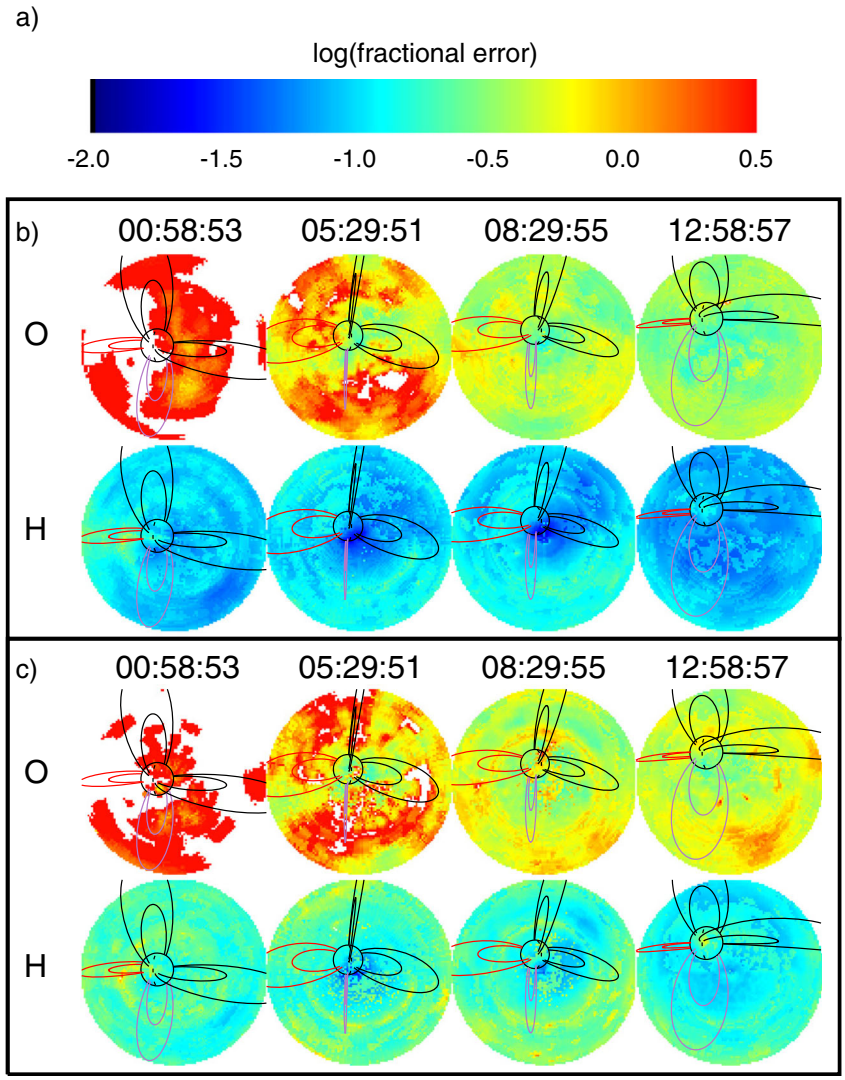

Figure 3. Map of the counting error is shown for each of the images in Figure 2. (a) The fractional error is defined as $1/\sqrt{n}$, where n is the number of scaled counts in a pixel. Since n is a fitted value, it is not required to be an integer value. Pixels colored white represent errors > 200% (less than 0.25 counts). (b) Error images for the ENA images in Figure 2b and (c) error in Figure 2c.

[33] During the recovery stage (1258 UT, Figure 2), the H ENA signal is greatly reduced from the peak of the storm, and the H LAE signal is nearly unobservable. Compared to the pre-storm images, the hydrogen HAE emissions are brighter than the LAE emissions. This may be an indication that the loss cone for H^+ has significantly emptied by this time. In contrast, the O ENAs are still significantly brighter in both the HAE and LAE than that observed in the pre-storm image. A distinct, pre-midnight O HAE is observed. More striking is that at this time, there is a very bright O LAE that was absent prior to the storm. This indicates that the loss cone still has significant O ions precipitating into the atmosphere. The lighter H ions will have 4 times shorter bounce period than O ions, assuming they have the same parallel energy. This shorter bound period may lead to more collisions in the upper atmosphere, and a more rapid empting of the loss cone. Also, the larger gyro radius of the O makes it more susceptible to pitch angle scattering which may be a source of refilling of the loss cone. Since the orbital positions for TWINS 1 at 01 and 13 UT are very similar, the viewing geometry effects on the observed LAEs should be minimal between these 2 times.

[34] To better quantify the temporal variation of the HAE and LAE, we calculate two indices as first done in *Valek et al.* [2010]. The indices defined here are modified from those used in *Valek et al.* [2010] to be more robust. The changes to the indices do not change the conclusions derived from *Valek et al.* [2010]. The HAE index is defined to be the average ENA flux measured where the line of sight passes between 2 and 4 Re from Earth. This gives a global overview of the ENA production in the ring current and most of the inner magnetosphere. By only including emissions outside 2Re, the bright LAEs are excluded from this index. By excluding emissions outside 4Re, we do not include pixels with the lowest count rates and therefore the highest pixels with the highest uncertainties from counting statistics. The HAE index is not adjusted for changes in latitude or other viewing geometry effects. To do so would

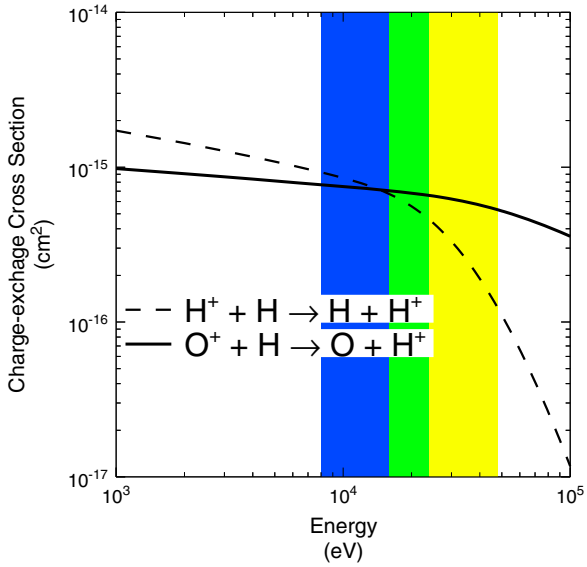

Figure 4. Charge exchange cross sections for H^+ and O^+ on H. The energy bands studied in this paper are shown in blue (16 keV) and yellow (32 keV), with the overlap in coverage shown in green.

require full image inversion or forward modeling, which we feel is beyond the scope of this paper.

[35] Since the LAEs are localized to near the Earth limb, the LAE index is calculated using data from inside 2Re. The LAE index is calculated as the mean of the 16 brightest pixels minus the mean of the remaining pixels inside of 2Re. This allows for the bright LAE to be separated from the any broader ENA signature or any backgrounds present across the whole image.

[36] The LAE and HAE indices for this storm are calculated from 30 min ENA images and are shown in Figure 7. The red curves are for the 16 keV energy band, and the blue for the 32 keV band. The solid (dashed) line is for H (O) in the HAE, LAE, and CRCM panels (2, 3, and 5), and the values increase as one moves downward on the y axis to allow for simpler comparison to the Sym-H values. The two time periods between 0600 to 0800 UT and 1200 to 1230 are regions with elevated backgrounds in the TWINS measurements and are not included in this study.

[37] The rate of increase of the HAE can be calculated as $\tau = \frac{1}{f}\frac{df}{dt} = \frac{d\ln f}{dt}$. During the period between 0300 and 0530 UT, the O HAE rate of increase is 1.5 times larger than that of the H HAEs at 16 keV and 2 times larger at 32 keV. During the main phase, a small but rapid increase in the AE index at 0300 UT is seen, which is consistent with a small substorm occurring at this time (Figure 1).The elevated rate of increase of O during this period is consistent with the observations of *Mitchell et al*. [2003] enhanced O injections during substorms. The rates of increase for the H and O HAEs are approximately equal during the rest of the period shown here. In the period between 0000 and 0230 UT, the measurement error for O is significant, so it is difficult to estimate of the O rate of increase during this time.

[38] A second dip in Sym-H for this storm is seen at 0900 UT. The O ENAs show a very slight increase, while the H continues to decrease in emissions. At 1000 UT, there is a sudden brightening of both the H and O HEAs. This is coincident with at rapid rebuilding event of the radiation belts [*Glocer et al*., 2011]. The images taken between 1000 and 1030 UT have enhanced backgrounds, which may result in an overestimate of the HAEs at those times, and are not included here. In both the LAEs and HAEs, this increase is larger in the H than in the O. This is most likely due to the background resulting from light particles (e.g., some local ions getting past the collimators). The light particles will skew the measure pulse height distribution to be more H-like.

[39] The slow recovery phase of the storm begins ~ 1200 UT. Both the H and O HAEs are elevated from the pre-storm levels and are gradually decaying. The O HAEs increased by a larger factor than the H HAEs. At the beginning of the recovery, the H LAEs are approximately at their pre-storm levels. The O LAEs, however, are approximately an order of magnitude more intense than the pre-storm levels.

[40] The average ENA flux is proportional to the average ion flux, described by the thin target approximation for HAEs

$$\langle J_{\mathrm{ion,HAE}} \rangle \propto \frac{1}{\sigma_{10}} \langle J_{\mathrm{ENA,HAE}} \rangle \tag{1}$$

where σ_{10} is the charge exchange cross section of the parent ion with the background H exosphere, plotted versus energy in Figure 4. The average ion flux in EQ 1 is over a line of sight integral. For simplicity, we assume that the parent ion populations for H and O have comparable line of sight distributions. Using this approximation, the ratio of the HAE parent ion populations of O to H are given in the fourth panel of Figure 7 (thick line). The pitch angle distributions of H^+ and O^+ can be quite different [*Daglis and Axford*, 1996], so the line of sight distributions of H^+ and O^+ may also be quite different. Local variations of the O/H ratio along the line of sight may deviate from the line of sight average plotted in Figure 7.

[41] *Bazell et al*. [2010] gave a thick target approximation (TTA) for a parent proton population on neutral oxygen generating H LAEs. However, a TTA has not been developed for a parent O^+ population on neutral oxygen generating O LAEs due to the complexity of the possible interactions. Because of this, a quantitative O / H ratio for the parent populations for the LAEs is unavailable since these relate to the ENA LAEs by an undetermined factor, which is itself a function of energy. Instead, we plot in the fourth panel of Figure 7 the ratio of O/H ENA LAEs, scaled to the value at 0200 UT (thin line), which we take as the start of the storm. This ratio allows us to observe the fractional change of the O/H LAE parent population.

[42] The ratio of the HAE parent ion population increases from ~1% pre-storm to ~ 10% O/H at the beginning of the early recovery. During this storm, the O component of the ENAs increases more rapidly and remains at elevated levels for a longer period of time than for H ENAs. The lower energy bin shows a larger increase than the higher energy bin. The ratio of the LAE ENA populations shows a larger fractional increase in O than the HAEs. The LAEs increase by an order of magnitude, whereas the HAEs increase by only a factor of ~ 3 to 5. This may be an indication of nonadiabatic heating of the O resulting in a pitch angle distribution that is more favorable for the production of LAEs.

[43] The bottom panel of Figure 7 shows CRCM [*Fok et al*., 2001]. Simulation results for the ring current total kinetic energy content for this event. We ran the CRCM for the period 1800 UT 21 July to 1800 UT 22 July 2009

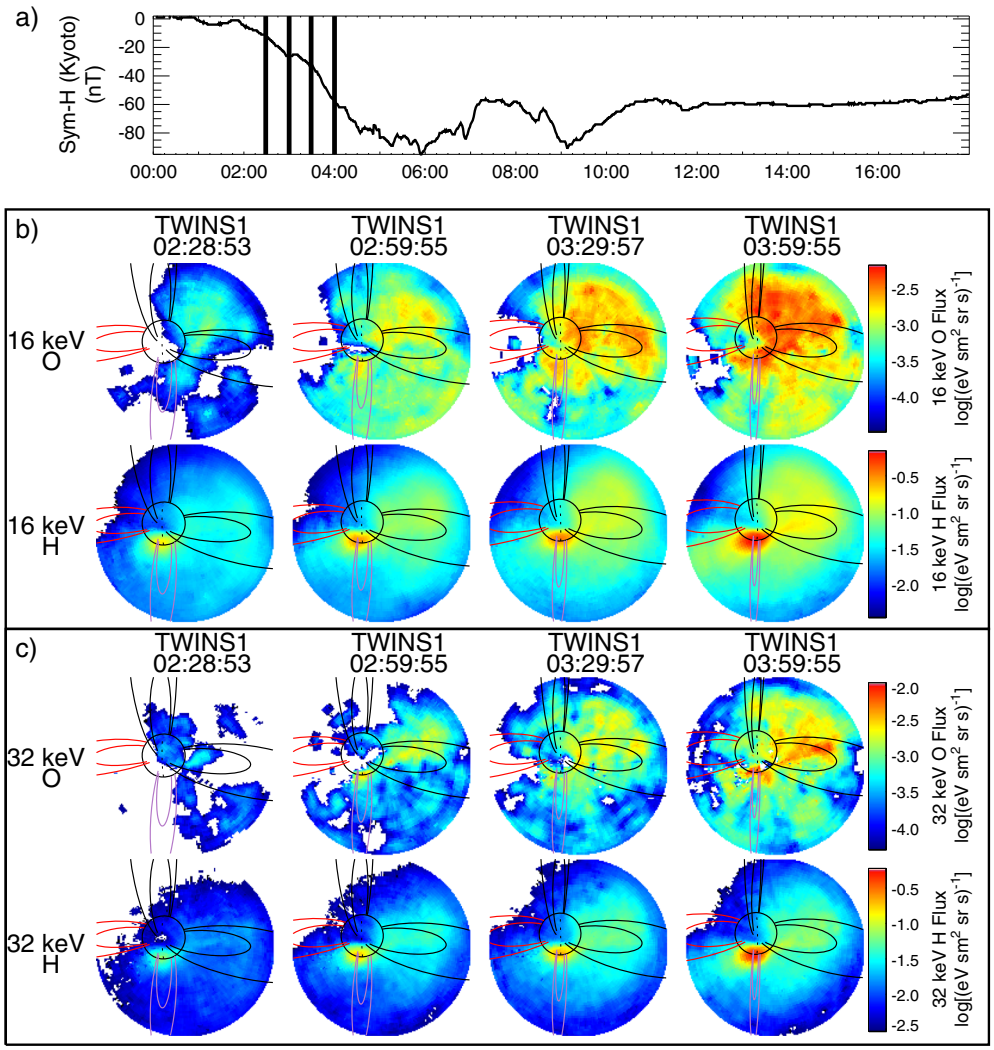

Figure 5. H and O ENA images during the storm main phase (same format as Figure 2). The ENAs shown are from a portion of the TWINS FOV cone with a half angle of 35° to highlight the near Earth emissions.

with the inputs as described in *Fok et al*. [2010] for static magnetic field case. The difference from the setup described in *Fok et al*. [2010] is that we also include an O^+ component with density calculated according to *Young et al*. [1982] relation. The Young relation specifies O^+/H^+ ratio for ion densities at the CRCM polar boundary as a function from Kp and F10.7 indices. For each species, we calculate the energy content by integrating CRCM-calculated number of particles in the entire CRCM computational domain inside ~9RE in the equatorial plane in a given TWINS energy bin. We believe this is a good proxy for ENAs because plasma at all L-shells contribute to bright ENA emissions near the Earth where geocorona density is high (with modulation from pitch angle distribution). Both O^+ and H^+ populations are subject to drift losses through magnetopause and charge-exchange losses. Charge-exchange cross-section energy dependence is different for O^+ and H^+ making different loss rates for different species with the same temperature.

[44] There is a general qualitative agreement between this result and the indices described above. Both show a rapid increase with the main storm phase, with gradual decay during the recovery phase. We observe also that O^+/H^+ ratio in the CRCM is smaller in the beginning of the storm and increases during main phase. This is consistent with *Young et al*. [1982] relation where O^+/H^+ ratio increases with activity. The CRCM model predicts a similar O/H ratio as we see in the HAEs (not shown).

[45] To determine detailed local time response, either a forward model [*Brandt et al*., 2001] or deconvolution [*Perez et al*., 2001] is required. This will be done in future studies, but for an approximate determination of the local time variation, we divide the HAE index describe above into local time sectors using the location where the line of sight crosses the magnetic equatorial plane; these four sectors are centered on 00, 06, 12, and 18. The resulting local time HAE index is shown in Figure 8.

[46] The local time HAE index for H shows increases in the ENAs on the night side, which then drift westward to the dusk side. During the peak of the storm, we see the ring current over a larger extent of local time. During the recovery phase, the ENAs are most intense on the night and dusk sides. For the O HAEs, during the main phase there is nearly an equal increase seen in the dawn and dusk sectors. We also note that

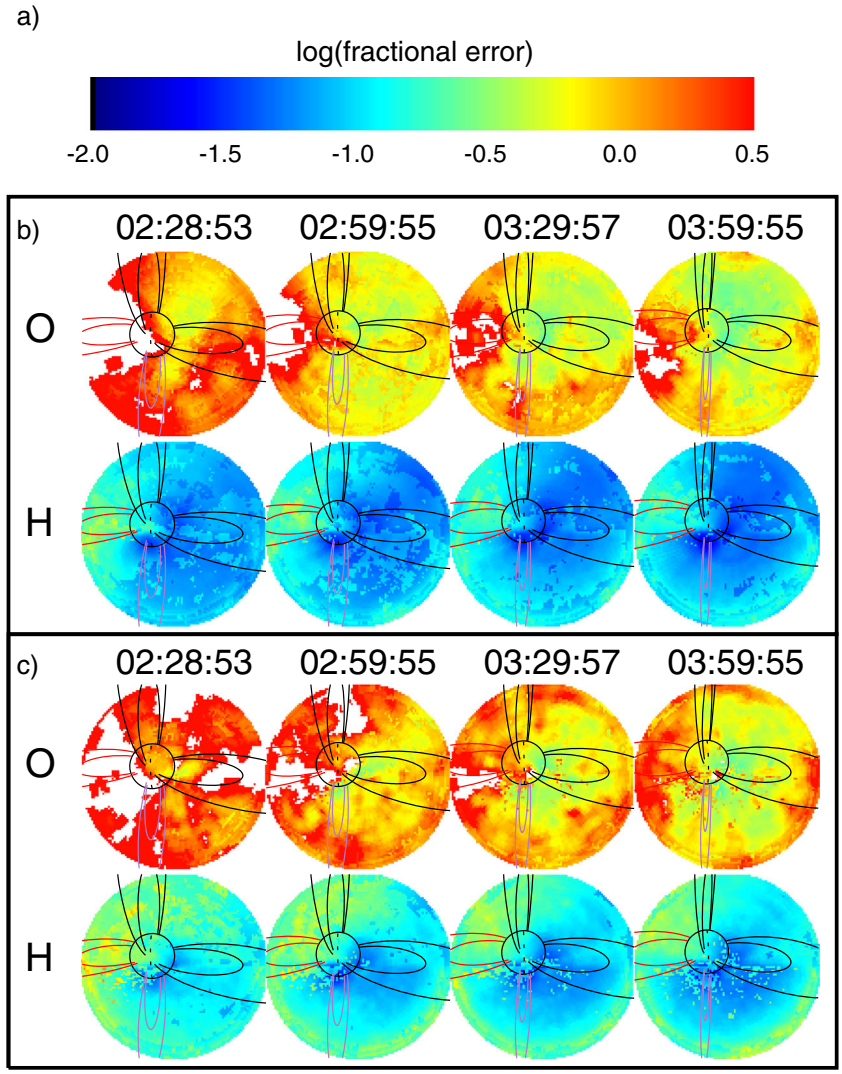

Figure 6. Map of the counting error is shown for each of the images in Figure 5. This figure has the same format as Figure 3.

the spreading of the 16 keV emissions from a concentration at midnight at 0300 UT toward dusk at 0600 UT is consistent with *Perez et al.* [2012, Figure 7].

4. Discussion and Conclusions

[47] Using the ENA imagers of the TWINS mission, we studied the variations in the global composition of the inner magnetosphere during the 22 July 2009 storm. This required developing and implementing a methodology to separate O from H ENAs. This technique is based on the mass dependent variation in the electron yield from the ultrathin carbon foils, manifested in the measured pulse height distributions. Using this technique in this paper, for the first time we

[48] 1. presented global O and H images of the inner magnetosphere centered on 16 and 32 keV ENAs (8–48 keV inclusive);

[49] 2. produced images with the spatial resolution needed to differentiate between H and O LAE and HAE ENAs;

[50] 3. identified local time differences in the evolution of H and O distributions during storm time for the inner magnetosphere in this critical energy range;

[51] 4. identified temporal differences in the evolution of H and O during different phases of the storm;

[52] 5. showed qualitative agreement between the H and O observations with model results from CRCM.

[53] While this storm has been studied by others [*Valek et al.*, 2010; *Fok et al.*, 2010; *Glocer et al.*, 2011; *Keesee et al.*, 2012; *Perez et al.*, 2012], we present the first measurements of the O component in the inner magnetosphere for this storm. The contribution of O^+ is expected to be small for this moderate storm [*Daglis and Axford*, 1996; *Fu et al.*, 2001].We observe that the O component is not a significant fraction of the ring current (O/H peaks at 0.1); however, we do have the sensitivity to observe that the O population evolves differently than the H population, both temporally and spatially.

[54] During the main phase of the storm from 0300 to 0530 UT, both the H and O HAEs increase rapidly. During this period, the 16 keV (32 keV) O HAEs have a rate of increase that is 1.5 (2.0) times larger than the H HAEs of the same energy. A strong H LAE is seen prior to the storm and through the main phase. The H LAEs then have a gradual

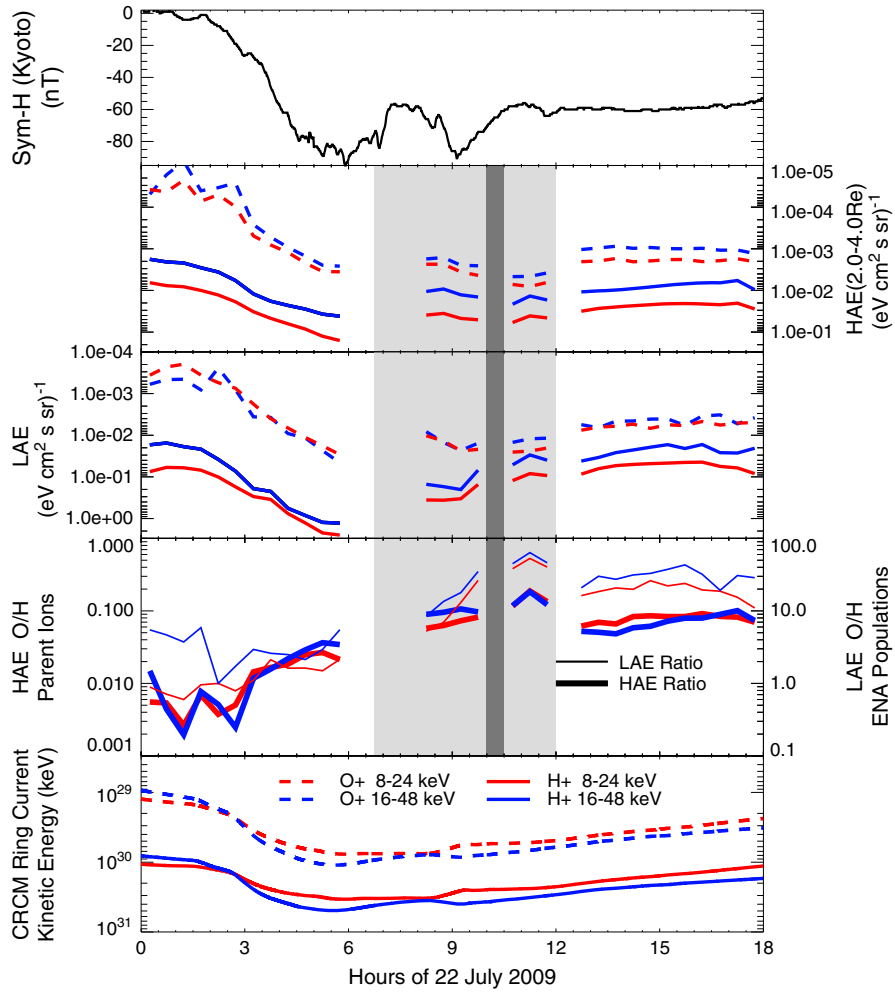

Figure 7. Overview of HAE and LAE indices (second and third panels, respectively). The 16 keV (32 keV) band is in red (blue). The H (O) observations use a solid (dashed) line. Included in the top panel is the Sym-H index for context. The ratio of O to H HAE ion parent populations (thick line) and LAE ENA populations (thin line) are shown in the fourth panel. The bottom panel shows results from a CRCM run of this event. The rapid rebuilding event reported by *Glocer et al.* [2011] is indicated by the dark gray bar at 1000 UT.

decrease down to below pre-storm levels at the start of the storm recovery at 1200 UT. In contrast, very few O LAEs are seen pre-storm, but they exhibit a rapid increase and peak at the same time during the storm as the H LAEs. At the early recovery phase of this storm, the O LAEs remain above the pre-storm levels, in contrast the H LAEs.

[55] The AE index rises rapidly by ~600 nT starting at 0300 UT, coincident with the largest rate of increase for the O ENAs. *Delcourt* [2002] showed that during substorm dipolarizations, low energy O^+ in the plasma sheet can be energized to high energy (100 keV) and be injected into the ring current. Using AE as a proxy for substorm activity, the observation of increased O HAEs during the increases in AE is consistent with the result of *Delcourt* [2002].

[56] The local time HAE index for H shows increases in the ENAs on the night side, which then drift westward to the dusk side. During the peak of the storm, we see the ring current is seen over a larger extent of local time. During the recovery phase, the ENAs are most intense on the night and dusk sides. For the O HAEs, during the main phase, there is nearly an equal increase seen in the dawn and dusk sectors. This may be indicative of the injected O ions traveling further earthward from the tail prior to drifting westward. During the recovery, the O/H ratio of the parent population is uniform in local time, with a larger relative increase for the lower energy band.

[57] Early studies [*Akasofu et al.*, 1963] of large magnetic storms showed that what is now referred to as the recovery phase consists of two parts, one with a rapid decay of a few hours and a second much slower and lasting much longer. Observations [*Hamilton et al.*, 1988] and simulations [*Noël*, 1997] of a great storm in February 1986 showed that O^+ was the dominant component in the energy density near the storm's main phase. The rapid decay phase was attributed to the loss of O^+ ions via charge exchange in the inner ring current. In contrast, *Ohtani et al.* [2005] reported that for a large storm in August 2000, IMAGE/HENA data suggested that both total H^+ and O^+ increased at the start of the recovery phase due to substorm activity. A statistical study [*Ohtani et al.*, 2006] of both H^+ and O^+ energy density during 59 storm events from September 2001 to March 2003 with Sym-H ≤ -50 nT confirmed that the 60–119 keV H

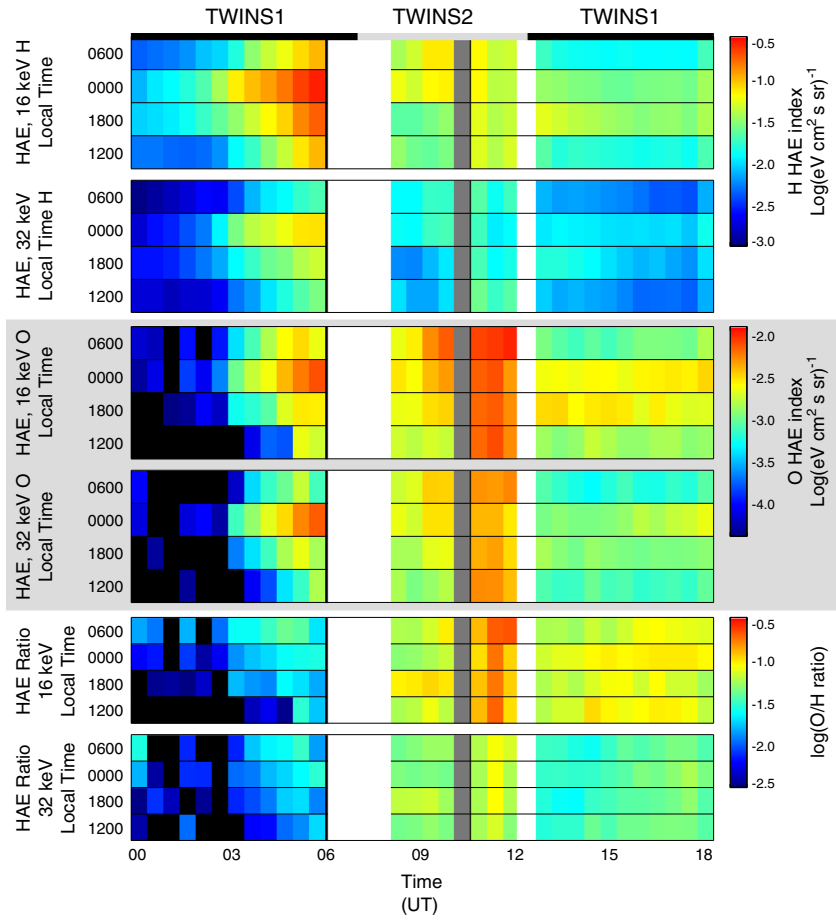

Figure 8. HAE variation with local time. The regions of elevated backgrounds highlighted in Figure 5 are indicated by the white boxes in this figure.

ENAs and the 52–180 keV O ENAs are stronger during the recovery phase of the storms. These authors also found that the O ENAs contribution relative to the H ENAs contribution increased with storm intensity.

[58] While this is a relatively weak storm, it is certainly in the range considered by *Ohtani et al.*, [2006]. The observations presented here are consistent with their findings that the substorm activity at this time shown in Figure 1 produces an increase in ENAs even as Sym-H increases. For the energy range we present here, the increase in the O/H ratio during the rapid recovery period is in sharp contrast to what was observed for very large storms. It should be noted that storms with very low Sym-H are usually ICME-driven storms, and the storm analyzed here is CIR driven. The relatively small contribution from the O^+ during most of the storm studied here is also consistent with expectations for relatively weak storms.

[59] Thus, we present here the methodology to produce and the first O ENA images measured by the TWINS ENA imagers. We also present for the first time the oxygen ENA images with high enough spatial resolution to resolve the localized Low Altitude Emissions separately from the high-altitude (largely ring current) emissions. While this study only shows the magnetosphere's global compositional response to one, rather small storm, importantly, it provides the methodology and techniques needed to separate H and O ENAs for future TWINS measurements and observations.

Appendix A: TWINS Composition Determination

[60] The TWINS instrument [*McComas et al.*, 2009] measures Energetic Neutral Atoms (ENAs) incident direction and velocity using a coincidence method. The ENAs that enter the TWINS aperture pass through an ultrathin carbon foil [*McComas et al.*, 2004] and liberate secondary electrons. The secondary electrons are accelerated toward the detector plane with ~1.1 kV acceleration potential. The microchannel plate (MCP) based sensor then measures the arrival time and position of the secondary electrons and the primary ENAs to determine the particles incident direction and velocity. See Figure A1 for a drawing of the geometry of the TWINS sensor heads. The interaction of the ENA and the foil does perturb the trajectories of the ENAs through angular scattering and energy straggling [*Funsten et al.*, 1993]. The perturbation of the ENAs velocity is a function of the particles mass and energy and results in an uncertainty in the ENA images [*Valek et al.*, 2010].

[61] For each coincident event measured, TWINS reports "Direct Events" (DEs). These DEs have the detailed information of the instrument response to the ENAs that allow us to produce map of the ENA population as a function of the arrival direction and energy per amu. Included in the direct events are the arrival location on the detector plane of the secondary electrons and primary ENA, referred to as the start position and

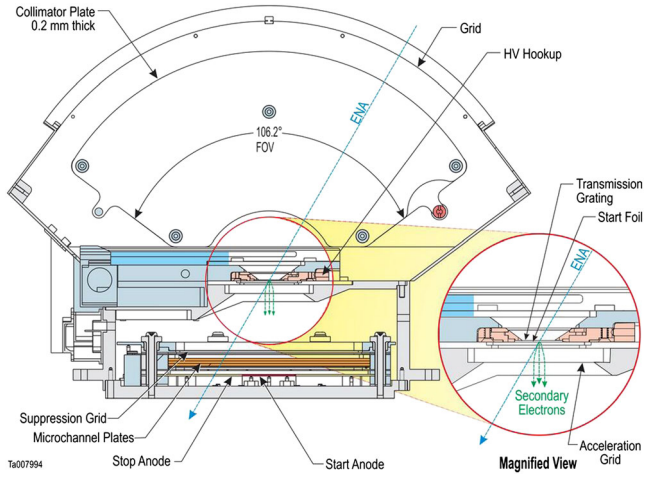

Figure A1. Figure showing the trajectories of the ENAs through a TWINS sensor.

stop position, respectively. The direction of travel inside the sensor is determined using these measured positions and the sensor geometry. Also included in the DEs is the time of flight (TOF) which is the time between the arrival of the secondary electrons and the primary ENA. Using the TOF, the direction of travel in the sensor, and the distance between the carbon foil and the detector plane, the ENAs velocity (inside the sensor) is determined. The direction and velocity of the ENA are then mapped to the most probable arrival direction and velocity of the ENAs prior to the carbon foils (see *McComas et al.* [2012] for a detailed discussion of the TWINS image making process).

A1. Determination of Composition From the Pulse Height Distribution

[62] For each secondary electron (start) and primary ENA (stop), TWINS measures the height of the pulse of electrons exiting from the MCP detectors. The size of the pulse height is a function of the incidents particles mass and energy. Starts (secondary electrons) have an energy nearly equal to the acceleration potential since the electrons exit the foil with an energy of only a few eV. The stops (primary ENAs) impact the detector with nearly the same energy as they entered the instrument since the perturbation of the foil is fairly small [*Allegrini et al.*, 2006] compared to the TWINS measurement range of 1 to 100 keV/amu.

[63] Past instruments, such as the IMAGE HENA instrument, used the measured pulse height of the primary ENA to determine its species [*Mitchell et al.*, 2003]. For the HENA instrument, the stop pulse heights have sufficient separation between H and O ENAs to be used to determine species. However, for the operating parameters used with the TWINS instrument, the distribution of pulse heights for O and H do not have enough separation to be used to determine species. Instead, the TWINS instrument uses the start pulse height to determine species.

[64] A small integer number of secondary electrons are liberated when the ENA transverses the carbon foil. The distribution of the number of electrons emitted is a function of the primary particles velocity and mass [*Gruntman et al.*, 1990; *Ritzau and Baragiola*, 1998].The secondary electrons are emitted from the foil with enough spread in their velocities that they have a separation at the detector plane that is large (~1 mm) compared to the hole spacing of the MCPs (~10 μm).

[65] Each electron from the foil therefore has a chance of generating its own charge pulse in the MCPs, which results in a pulse that can be estimated as n*C, where n is the number of electrons from the foil and C is the average charge pulse per electron. While the average pulse height for O is larger than that of H, the pulse height distributions for H and O are both fairly wide and have significant overlap for the TWINS detectors. This is due to both the variation of the number of electrons emitted from the foil per incident ENA and the width of the pulse height distributions as a function of the number of electrons striking the MCP. Thus, one is unable to determine the mass of individual ENAs using the start pulse height; however for a large enough collection of ENAs, one can statistically determine the relative fractions of H and O.

[66] The start pulse height distributions for H (red) and O (green) for particles with energy per mass of 2.7 keV / amu are shown in Figure A2. Both curves have been normalized so the total area under each curve is equal. Vertical dashed lines are at the approximate locations of the peak of the 1, 2, 3, and 4 electron pulse height distributions. The resultant H and O distribution are the combination of the n-electron distributions

$$PH_i = \sum_n \alpha_{i,n} \cdot ph_n \tag{A1}$$

where PH_i is the total start pulse height for species i, ph_n is the start pulse height if n electrons are emitted from the foil, and $\alpha_{i,n}$ is the probability that n electrons are emitted from the foil for species i.

[67] Figure A3 shows the variation of the PH distributions as the particle energy per mass was varied during the instrument flight calibration. The color of each trace indicates the total energy of the incident particle. The solid curves are for H^+, and the dashed lines are for O^+. The majority of the TWINS calibration was performed with ions since the instrument performance is identical except for the ion rejection subsystem and a small (~ 1 kV) potential at the foil with will increase the energy of the incident ion.

[68] The difference in the start pulse height distributions is used to determine the fraction of H and O measured by TWINS. Using pulse height distributions determined during the instrument calibration, PH_H and PH_O, the measured start pulse height distribution can be written as the linear combination

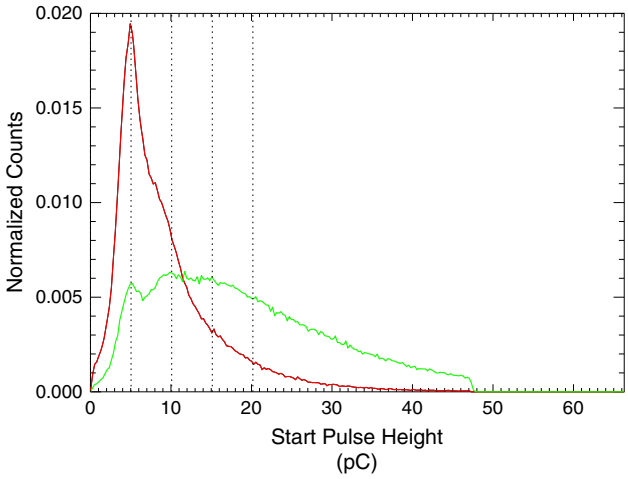

Figure A2. Comparisons of the start pulse height distributions for H (red) and O (green) that enter the sensor with nearly the same velocity. The start pulses are from secondary electrons emitted from ultrathin carbon foils.

$$PH_T(x) = A{\cdot}PH_H(x) + (1 - A){\cdot}PH_O(x) \tag{A2}$$

where PH_T is the measured normalized pulse height of combined H and O ENAs, A is the fraction of events that are from H ENAs, and x indicates which bin of the distribution (i.e., the charge exiting the detector). This parameter A is the fraction of H ENAs measured by TWINS prior to the application of mass specific response functions for TWINS and not the fraction of incident H ENA flux into TWINS. The value of A in equation A2 is determined by performing a least squares fit. Any measurement of y events of pulse height x will have some measurement error, so the residual for each is given by

$$\begin{aligned} r_i &= y_i - PH_T(x_i) \\ &= y_i - A{\cdot}[PH_H(x_i) - PH_O(x_i)] - PH_O(x_i) \end{aligned} \tag{A3}$$

[69] The least squares solution provides the value where A minimizes the value of χ^2, where

$$\chi^2 = \sum_i \frac{(y_i - A{\cdot}[PH_H(x_i) - PH_O(x_i)] - PH_O(x_i))^2}{\sigma_i^2} \tag{A4}$$

where σ_i is the standard deviation of the measurement error. Assuming our measurement is described by a Poisson distribution, the standard deviation can be estimated by $\sigma_i = \sqrt{y_i}$. For bins that measure 0 events, we use a standard deviation of 1 count. Since A is the fraction of counts due to H, we impose the condition that $0 \le A \le 1$. If any values of $A < 0$ are set to 0, and any values of $A > 1$ are set to 1.

[70] Helium is not included in the composition determination. The helium-electron yield, and therefore the pulse height distribution, is between that of H and O. However, the production of He ENAs is significantly less efficient than that for H or O. The charge exchange cross sections for He^+ on H is about a factor of 2 lower than the charge exchange cross section of H^+ on H at 16 or 32 keV/amu [*Barnet*, 1990]. So even if He^+ was found in quantities of say 10% compared to H^+ in the inner magnetosphere, the He ENA signal would be only ~1%.

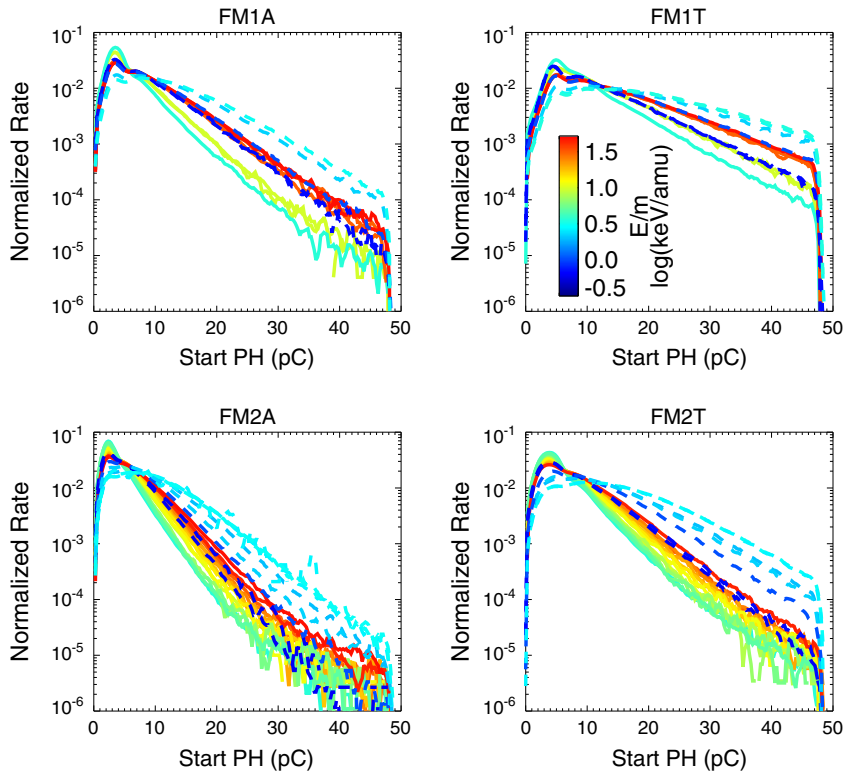

Figure A3. The PH distributions vary with both E/m and species. Shown here for the four sensor heads that make up the two TWINS instruments are the measured pulse height distributions during calibration. Solid curves indicate H, and dashed curves indicate O. The E/m of the curves is indicated by its color.

A2. Extrapolation of the Pulse Height Distribution

[71] The facility used for the TWINS calibration [*McComas et al.*, 2009] has an ion source with an energy range between 1 and 50 keV. Because of this, there is only a limited overlap in energy per mass between H^+ and O^+ used during calibration. To extend the range where the composition fractions can be determined, the H^+ (O^+) pulse height distributions must be extrapolated to lower (higher) energy per mass.

[72] The pulse height distribution is modeled as a summation of Gaussians

$$PH_S(v,m) = \sum_{n=1}^{\infty} P_{S,n}(v,m)\left[C_{S,n}\cdot e^{\left(-\frac{1}{2}\left(\frac{(x-\alpha_{S,n})}{\sigma_{S,n}}\right)^2\right)}\right] \quad \text{(A5)}$$

where v and m are the incident particles velocity and mass, and the index s indicates which of the four TWINS sensors (two sensors per spacecraft) the distribution applies to. The summation is over the number of electrons, n, starting cascades in the MCPs. The second term (in brackets) in the summation describes the pulse height distribution when n electrons start cascades in the MCP, with x being the pulse height and $\alpha_{s,n}$ the location of the n electron peak (e.g., 5 pC in Figure A2). The values of $\alpha_{s,n}$ and $\sigma_{s,n}$ are independent of v or m, since all electron emitted from the carbon foil are accelerated to the same potential. The first term in the summation, $P_{s,n}(v,m)$, is the probability that for an incident particle with velocity v and mass m will emit n electrons which start cascades and is modeled with a Poison distribution

$$P_{S,n}(v,m) = \frac{q_s(v,m)^n}{n!}e^{-q_s(v,m)} \quad \text{(A6)}$$

where $q_s(v,m)$ is the effective yield from the carbon foil in sensor s, for incident particles with velocity v and mass m.

[73] The effective yield will differ from the actual secondary electron yield from the carbon foil since the MCP detectors do not measure the incident electrons with a 100% efficiency. The number of electrons contributing to the measured pulse height distribution, n, will be less than or equal to the number of electrons emitted from the carbon foil, n' ($n \le n'$). In addition, the most probable number of electrons emitted from the carbon foil is 0 [*Gruntman et al.*, 1990]; however, it is obvious that the TWINS MCP detectors can only measure an electron when one is emitted from the foil and therefore cannot estimate the fraction of incident events which do not emit electrons from the foil. Therefore, the effective yield inferred from the TWINS pulse height distributions will differ from published values for the forward electron yield from 0.5 $\mu g\,cm^2$ carbon foils [*Allegrini et al.*, 2003; *Ritzau and Baragiola*, 1998].

[74] The measured pulse height distributions can be fit to the model in equation (A3) to determine the only free parameter, the effective electron yield. Figure A4 shows examples of two such fits. The model given here does an excellent job reproducing the measured pulse height distributions.

[75] From the fits, we are able to determine the relation between the effective yield ($q_s(v,m)$) and the incident particles energy per mass. This is shown in Figure A5, with the H (O)

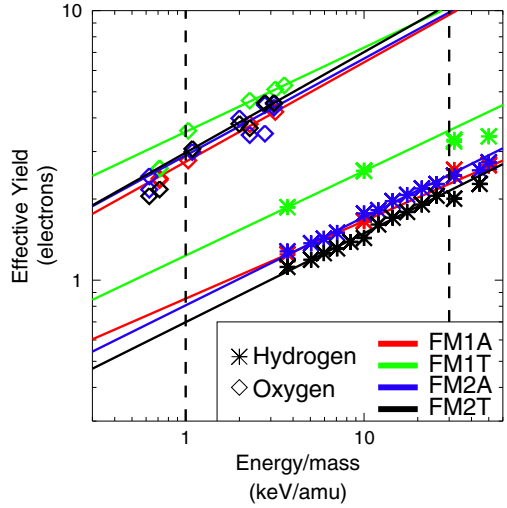

Figure A5. Effective electron yield inferred from the pulse height distributions. The vertical dashed lines indicate region of highest confidence of the extrapolations. See text for description.

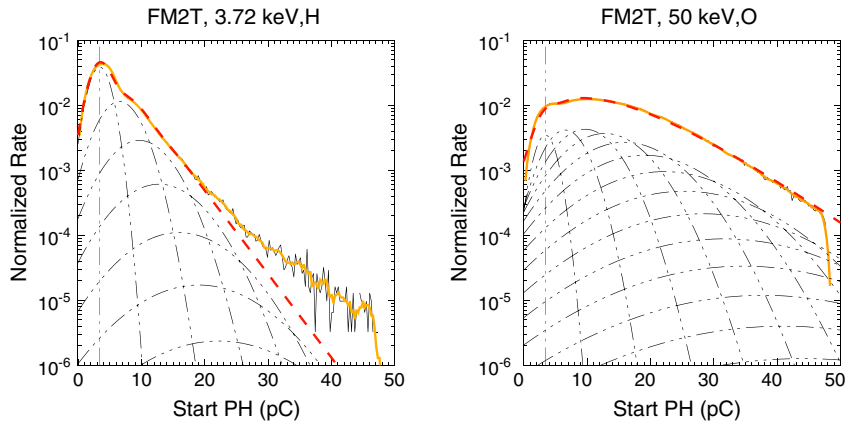

Figure A4. Examples of fitting the calibration data to the model describe in equation (A3). Measured pulse height distributions are shown with the thin black line, with smoothed values overlaid (orange curve). Individual n-electron distributions are shown in the dash-dot lines, with the accumulative fit drawn with the red dashed line.

data indicated with starts (diamonds). While the yields are lower than published by others [*Allegrini et al.*, 2003; *Ritzau and Baragiola*, 1998, and references therein], the shapes of the curves do agree with those results.

[76] In the energy per mass range from 1 to ~30 keV/amu, the electron yield has been reported to vary with $(E/m)^{\beta}$, where β is near 0.5 [*Ritzau and Baragiola*, 1998]. For E/m below 1 keV/amu, straggling in the foil limits the yield. For E/m larger than ~30 keV/amu, stopping power goes down, also reducing the electron yield. Because of this, the pulse height model (equation (A3)) is only valid in this energy range.

[77] Using the best fit for the effective yield (Figure A5), we can now extrapolate the expected H and O pulse height distributions over the full energy/mass range of the TWINS

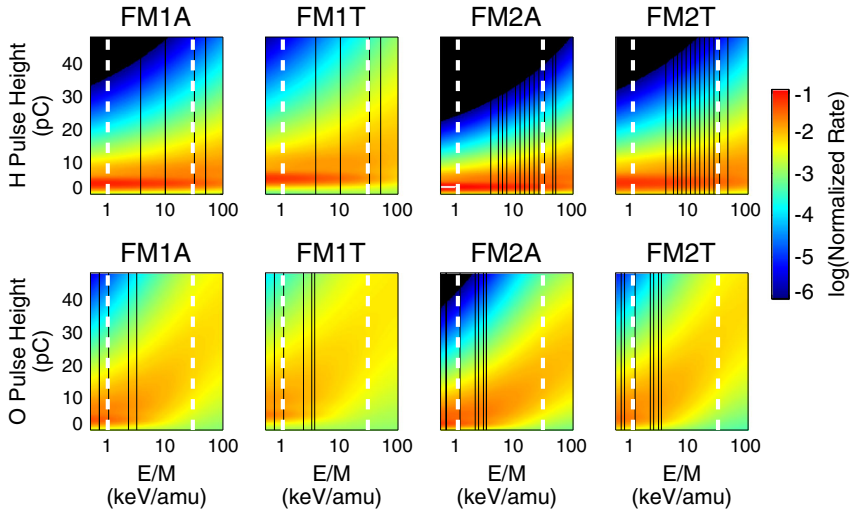

Figure A6. Extrapolated pulse height distributions using the results from Figure A6 and equation (A3). The white dashed lines bound the region where this extrapolation is valid, and the vertical black lines indicate the E/M where we have calibration data to constrain the model.

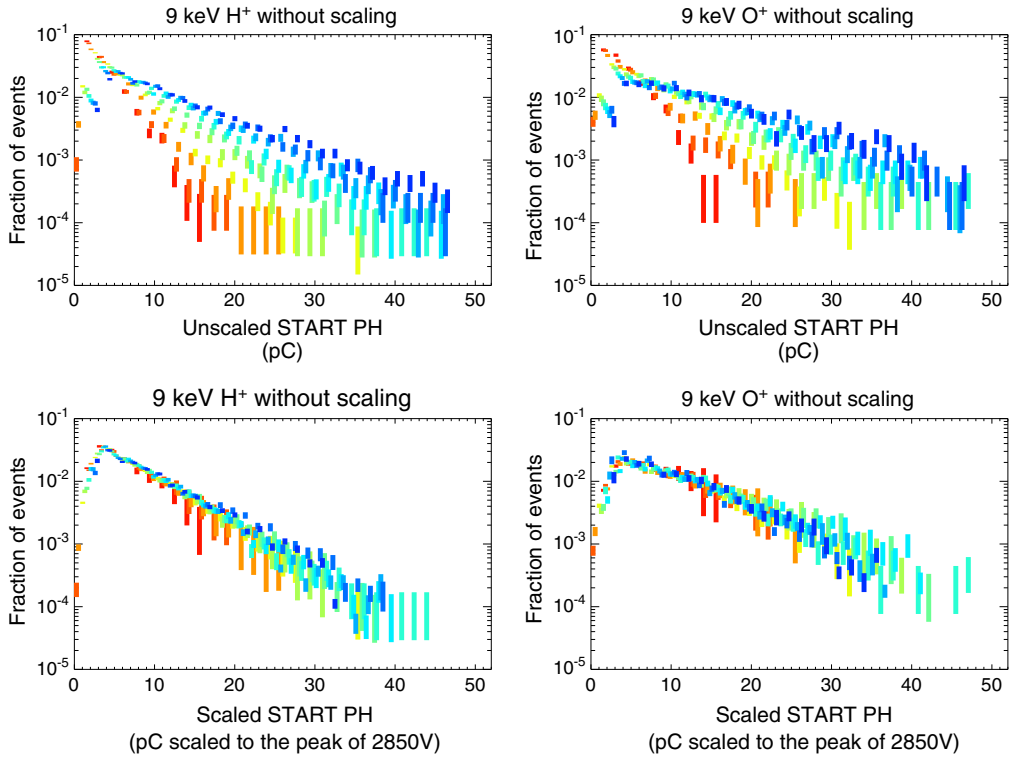

Figure A7. Pulse height distributions for varying MCP voltage. The color of the vertical bars indicate the MCP voltage, ranging from 2400 V (red) to 3200 V (dark blue). The length of the lines indicate ± 1σ counting error range from Poison statistics. The top panels show un-scaled pulse height distributions and the bottom panels show pulse height distributions scaled to the 1-electron peak with the MCPs at 2850 V.

instrument. The result of this extrapolation is shown in Figure A6, where the vertical black lines indicate points where there is calibration data to constrain the extrapolation.

A3. Gain Variation

[78] Over the life of a mission, the gain of MCP detectors gradually decreases. By design, this can be corrected by increasing the applied high voltage. For the TWINS mission, decrease in gain of the detectors has been observed. The MCP high voltage was increased March 2011 to return the gain to near launch levels. However, between voltage adjustments, this variation of the gain needs to be addressed when determining the composition, using equation (A2). The pulse height distribution is scaled such that the one electron peaks for the calibration data and the in flight measurement are aligned.

[79] Figure A7 shows the normalized pulse height distributions for an incident beam with energy of 9 keV measured during instrument calibration. The full pulse height distribution was measured for varying MCP voltages, ranging from 2400 V to 3200 V in order to characterize the variation with MCP gain. The two panels on the left are for an incident beam of protons, and the two panels on the right are for an incident of O^+ ions.

[80] The top panels of Figure A7 show the pulse height distributions prior to any scaling. As the voltage is increased, the gain can clearly be seen to increase with MCP voltage as the distribution clearly shifts to having larger pulses. The bottom panels have their distributions scaled such that the 1 electron peaks align with the peak at 2850 V (nominal operating voltage). The scaled pulse height bytes for voltage v are

$$PH_{\text{scaled byte}} = PH_{\text{unscaled byte}} \cdot \left(peak\_byte_{2850} \Big/ peak\_byte_{v} \right) \quad \text{(A7)}$$

[81] Once the scaling is applied, the pulse height distributions are aligned to within the measurement error. This scaling is applied prior to performing the fit to determine the factor A in equation (A2). The parameter A then is used to determine the number of O and H counts measured in TWINS. Finally, species specific instrument response factors are applied to generate the composition separated images, such as in Figures 2 and 5 of the main text of this paper. See *McComas et al*. [2012] for a complete discussion on the TWINS image making process.

[82] **Acknowledgments.** This work was supported by the TWINS mission, which is a part of NASA's Explorer program. We thank the World Data Center for Geomagnetism, Kyoto for suppling Real Time Dst and AE indices. We also thank the ACE and Wind plasma and magnetometer teams for L1 data and the OMNI data set for their propagation of these data.

References

Akasofu, S.-I., S. Chapman, and D. Venkatesan (1963), The main phase of great magnetic storms, *J. Geophys. Res.*, *68*, 3345.

Allegrini, F., R. F. Wimmer-Schweingruber, P. Wurz, and P. Bochsler (2003), Determination of low-energy ion-induced electron yields from thin carbon foils, *NIMB*, *211*(4), 487–494, doi:10.1016/S0168-583X(03)01705-1.

Allegrini, F., D. J. McComas, D. T. Young, J.-J. Berthelier, J. Covinhes, J.-M. Illiano, J.-F. Riou, H. O. Funsten, and R. W. Harper (2006), Energy loss of 1–50 keV H, He, C, N, O, Ne, and Ar ions transmitted through thin carbon foils, *Rev. Sci. Inst.*, *77*(4), 044501, doi:10.1063/1.2185490.

Angelopoulos, V. (2008), The THEMIS mission, *Space Sci. Rev.*, *141*(5), 5–34. doi:10.1007/s11214-008-9336-1.

Barnett, C. F. (Ed.) (1990), *Atomic data for fusion. Volume 1: Collisions of H, H2, He, and Li atoms and ions with atoms and molecule*, *ORNL-6086*, vol. 1, Controlled Fusion Atomic Data Center.

Bazell, D., E. C. Roelof, T. Sotirelis, P. C. Brandt, H. Nair, P. Valek, J. Goldstein, and D. McComas (2010), Comparison of TWINS images of low-altitude emission of energetic neutral atoms with DMSP precipitating ion fluxes, *J. Geophys. Res.*, *115*, A10,204, doi:10.1029/2010JA015644.

Brandt, P. C., S. Barabash, E. C. Roelof, and C. J. Chase (2001), Energetic neutral atom imaging at low altitudes from the Swedish microsatellite Astrid: Observations at low (< 10 keV) energies, *J. Geophys. Res.*, *106*(A11), 24,663–24,674, doi:10.1029/2000JA900119.

Burch, J. L. (2000), Image mission overview, *Space Sci. Rev.*, *91*, 1–14.

Buzulukova, N., J. G. M.-C. Fok, P. V. D. J. McComas, and P. C. Brandt (2010), Ring current dynamics in moderate and strong storms: Comparative analysis of TWINS and IMAGE/HENA data with the comprehensive ring current model, *J. Geophys. Res.*, *115*, A12,234, doi:10.1029/2010JA015292.

Daglis, I. A., E. T. Sarris, and B. Wilken (1993), AMPTE/CCE CHEM observations of the ion populations at geosynchronous altitudes, *Ann. Geophys.*, *11*, 685.

Daglis, I. A., and W. I. Axford (1996), Fast ionospheric response to enhanced activity in geospace: Ion feeding of the inner magnetotail, *J. Geophys. Res.*, *101*(A3), 5047–5065, doi:10.1029/95JA02592.

Daglis, I. A. (1997), chap. The role of magnetosphere-ionosphere coupling in magnetic storm dynamics, Magnetic Storms; AGU Monograph 98, pp. 107–116, AGU, Washington, D. C.

Delcourt, D. C. (2002), Particle acceleration by inductive electric fields in the inner magnetosphere, *JASTP*, *64*, 551–559.

Fok, M.-C., R. A. Wolf, R. W. Spiro, and T. E. Moore (2001), Comprehensive computational model of Earth's ring current, *J. Geophys. Res.*, *106*(A5), 8417–8424, doi:10.1029/2000JA000235.

Fok, M. C., T. E. Moore, P.C. Brandt, D. C. Delcourt, S. P. Slinker, and J. A. Fedder (2006), Inpulsive enhancements of oxygen ions during substorms, *J. Geophys. Res.*, *111*, A102,222, doi:10.1029/2006JA011839.

Fok, M.-C., N. Buzulukova, S. H. Chen, P. W. Valek, J. Goldstein, and D. J. McComas (2010), Simulation and TWINS observations of the 22 July 2009 storm, *J. Geophys. Res.*, *115*, A12,231, doi:10.1029/2010JA015443.

Fu, S. Y., Q. G. Zong, B. Wilken, and Z. Y. Pu (2001), Temporal and spatial variation of the ion composition in the ring current, *Space Sci. Rev.*, *95*, 539–554.

Funsten, H. O., D. J. McComas, and B. L. Barraclough (1993), Ultrathing foils for low-energy neutral atom imaging of the terrestrial magnetosphere, *Opt. Eng.*, *32*(12), 3090–3095.

Glocer, A., G. To'th, T. Gombosi, and D. Welling (2009a), Modeling ionospheric outflows and their impact on the magnetosphere, initial results, *J. Geophys. Res.*, *114*(A13), A05216, doi:10.1029/2009JA014053.

Glocer, A., G. Toth, Y. Ma, T. Gombosi, J.-C. Zhang, and L. M. Kistler (2009b), Multifluid Block-Adaptive-Tree Solar wind Roe-type Upwind Scheme: Magnetospheric composition and dynamics during geomagnetic storms: Initial results, *J. Geophys. Res.*, *114*(A13), A12203, doi:10.1029/2009JA014418, 200.

Glocer, A., M. C. Fok, T. Nagai, G. Toth, T. Guild, and J. Blake (2011), Rapid rebuilding of the outer radiation belt, *J. Geophys. Res.*, *116*, doi:10.1029/2011JA016516.

Goldstein, J., P. Valek, D. J. McComas, and J. Redfern (2012a), Latitudinal anisotropy in ring current energetic neutral atoms, *Geophys. Res. Lett.*, *39*, L08102, doi:10.1029/2012GL051417, in press.

Goldstein, J., P. Valek, D. J. McComas, and J. Redfern (2012b), TWINS energetic neutral atom observations of local-time-dependent ring current anisotropy, *J. Geophys. Res.*, *117*, A11213, doi:10.1029/2012JA017804.

Gonzalez, W., J. Joselyn, Y. Kamide, H. W. Kroehl, G. Rostoker, B. T. Tsuruntani, and V. M. Vasyliunas (1994), What is a geomagnetic storm?, *J. Geophys. Res.*, *99*, 5771–5792.

Gruntman, M. A., A. A. Kozochkina, and V. B. Leonas (1990), Many-electron secondary emission of thin foils bombarded by accelerated atomic beams, *JETP Lett.*, *51*(1), 22–25, translated by A. Peiperl.

Hamilton, D. C. G., F. M. Gloeckler, W. Ipavich, B. W. Stüdemann, and G. Kremser (1988), Ring current development during the great geomagnetic storm of February 1986, *J. Geophys. Res.*, *93*, 14,343.

Keesee, A. M., J. G. Elfritz, D. J. McComas, and E. E. Scime (2012), Inner magnetosphere convection and magnetotail structure of hot ions imaged by ENA during a HSS-driven storm, *J. Geophys. Res.*, *117*, doi:10.1029/2011JA017319.

Lindsay, B. G., and R. F. Stebbings (2005), Charge transfer cross sections for energetic neutral atom data analysis, *J. Geophys. Res.*, *110*, A12,213, doi:10.1029/2005JA011298.

McComas, D. J., H. Funsten, and E. Scime (1998), chap. Advances in low-energy neutral atom imaging, *Measurement Techniques in Space Plasma: Fields*, *Geophys. Monogr. Ser.*, vol. 103, pp. 275–280, AGU, Washington, D. C.

McComas, D. J., F. Allegrini, C. J. Pollock, H. O. Funsten, S. Ritzau, and G. Gloeckler (2004), Ultrathin (10 nm) carbon foils in space instrumentation, *Rev. Sci. Inst.*, *75*(11), 4863–4870, doi:10.1063/1.1809265.

McComas, D., et al. (2009), The Two Wide-angle Imaging Neutral-atom Spectrometers (TWINS) NASA mission-of-opportunity, *Space Sci. Rev.*, *142*, 157–231, doi:10.1007/s11214-008-9467-4.

McComas, D., N. Buzulukova, M. Connors, M. Dayeh, J. Goldstein, H. O. Funsten, S. Fuselier, N. A. Schwadron, and P. Valek (2012), Two Wide-Angle Imaging Neutral-Atom Spectrometers and Interstellar Boundary Explorer energetic neutral atom imaging of the 5 April 2010 substorm, *J. Geophys. Res.*, *117*, A03,225, doi:10.1029/2011JA017273.

Mitchell, D., P. C. son Brandt, E. Roelof, D. Hamilton, K. Retterer, and S. Mende (2003), Global imaging of O + from IMAGE/HENA, *Space Sci. Rev.*, *109*, 63–75, doi:10.1023/B:SPAC.0000007513.55076.00.

Mitchell, D. G., C. P. Paranicas, B. H. Mauk, E. C. Roelof, and S. M. Krimigis (2004), Energetic neutral atoms from Jupiter measured with the Cassini magnetospheric imaging instrument: Time dependence and composition, *J. Geophys. Res.*, *109*, A09S11, doi:10.1029/2003JA010120.

Noël, N. (1997), Decay of the magnetospheric ring current: A Monte Carlo simulation, *J. Geophys. Res.*, *102*, 2301.

Ohtani S., P. C. Brandt, D. G. Mitchell, H. Singer, M. Nosé, G. D. Reeves, S. B. Mende (2005), Storm-substorm relationship: Variations of the hydrogen and oxygen energetic neutral atom intensities during storm-time substorms, *J. Geophys. Res.*, *110*, A07219, doi:10.1029/2004JA010954

Ohtani, S., P. C. Brandt, H. J. Singer, D. G. Mitchell, E. C. Roelof (2006), Statistical characteristics of hydrogen and oxygen ENA emission from the storm-time ring current, *J. Geophys. Res.*, *111*, A06209, doi:10.1029/2005JA011201.

Perez, J., G. Kozlowski, P. C. Brandt, D. G. Mitchell, J. M. Jahn, C. J. Pollock, and X. X. Zhang (2001), Initial ion equatorial pitch angle distributions from medium and high energy neutral atom images obtained by IMAGE, *Geophys. Res. Lett.*, *28*(6), 1155–1158, doi:10.1029/2000GL012636.

Perez, J. D., E. W. Grimes, J. Goldstein, D. J. McComas, P. Valek, and N. Billor (2012), Evolution of CIR storm on 22 July 2009, *J. Geophys. Res.*, *117*, A09221, doi:10.1029/2012JA017572

Pollock, C., et al. (2000), Medium energy neutral atom (MENA) imager for the IMAGE mission, *Space Sci. Rev.*, *91*, 113–154, doi:10.1023/A:1005259324933.

Pollock, C. J., A. Isaksson, J. M. Jahn, F. Soraas, and M. Sorbo (2009), Remote global-scale observations of intense low-altitude ENA emissions during the halloween geomagnetic storm of 2003, *Geophys. Res. Lett.*, *36*, L19,101.

Ritzau, S. M., and R. A. Baragiola (1998), Electron emission from carbon foils induced by keV ions, *Phys. Rev. B*, *58*(5), 2529–2538.

Roelof, E. C. (1997), ENA emission from nearly-mirroring magnetospheric ions interacting with the exosphere, *Adv. Space Res.*, *20*(3), 361–366, doi:10.1029/0273-1177/97.

Tsurutani, B. T., et al. (2006), Corotating solar wind streams and recurrent geomagnetic activity: A review, *J. Geophys. Res.*, *111*, A07S01, doi:10.1029/2005JA011273.

Valek, P., P. C. Brandt, N. Buzulukova, M. C. Fok, J. Goldstein, D. J. McComas, J. D. Perez, E. Roelof, and R. Skoug (2010), Evolution of low-altitude and ring current ENA emissions from a moderate magnetospheric storm: Continuous and simultaneous TWINS observations, *J. Geophys. Res.*, *115*, A11,209, doi:10.1029/2010JA015429.

Welling, D. T., V. K. Jordanova, S. G. Zaharia, A. Glocer, and G. Toth (2011), The effects of dynamic ionospheric outflow on the ring current, *J. Geophys. Res.*, *116*, doi:10.1029/2010JA015642.

Young, D. T., H. Balsiger, and J. Geiss (1982), Correlations of magnetospheric ion composition with geomagnetic and solar activity, *J. Geophys. Res.*, *87*, 9077–9096.

Zhang, J. M., W. Liemohn, J. U. Kozyra, B. J. Lynch, and T. H. Zurbuchen (2004), A statistical study of geoeffectiveness of magnetic clouds during high solar activity years, *J. Geophys, Res.*, *109*, A09101, doi:10.1029/2004JA010410.

Zhang, J. M., W. Liemohn, J. U. Kozyra, M. F. Thomsen, H. A. Elliott, and J. M. Weyhand (2006), A statistical comparison of solar wind sources of moderate and intense geomagnetic storms at solar minimum and maximum, *J. Geophys, Res.*, *111*, A01104, doi:10.1029/2005JA011065.

Erratum

In the originally published version of this article, the surname of Raluca Ilie was misspelled. The typographical error has since been corrected, and this version may be considered the authoritative version of record.